Journal of Building Engineering 64 (2023) 105733

Contents lists available at ScienceDirect

Journal of Building Engineering

journal homepage: www.elsevier.com/locate/jobe

Mineralogical and microstructural changes in alkali-activated and hybrid materials exposed to accelerated leaching

S. Shagñay [a,*], I. Garcia-Lodeiro [b], F. Velasco [a], A. Bautista [a], M. Torres-Carrasco [a]

[a] Materials Science and Engineering Department-IAAB, University Carlos III of Madrid, Avda. Universidad 30, 28911, Leganés, Madrid, Spain
[b] Eduardo Torroja Institute for Construction Science (IETcc-CSIC), Madrid, Spain

ARTICLE INFO

Keywords:
Geopolymers
Hybrid cements
Accelerated leaching
Microstructure
Durability

ABSTRACT

Alkali-activated materials (AAM) and hybrid cements (HC) have become sustainable alternatives to Portland cement (PC) due to their low carbon footprint. The main differences between AAM and HC lie in their content of clinker (none in the AAM and usually lower than 30% for HCs) and the type of activator used (strong alkaline solutions for AAM and small amounts of solid alkalis for HC). Durability problems related with microstructural changes due to decalcification and leaching of the cementitious paste have been well researched for PC pastes, but it is still not well known for AAM and HC. The present work aims to study the leaching process for cement pastes of both types of sustainable pastes.

Blast furnace slag (BFS) was selected as a precursor to manufacture hybrid slag (HS) pastes and alkali-activated slag (AAS) pastes. A commercial CEM IV was selected as reference material. A 6 M NH_4NO_3 solution was used to accelerate leaching kinetics. After 28 days of immersion, the mineralogical and microstructural changes were evaluated.

Results show that AAS pastes exhibited the highest leaching resistance of all the pastes under study, due to the absence of portlandite and the high level of polymerization of silicate chains. In HS pastes, the presence of portlandite (due to PC in the material) and gypsum (due to the activator) explains their intermediate performance, in between CEM IV and AAS.

1. Introduction

The global environmental situation has triggered a strong interest in the development of alternative cementitious materials, different to ordinary Portland cement (PC). The PC industry emits between 7 and 9% of CO_2 emissions [1,2]. In addition, its manufacturing involves high electrical energy consumption [3,4]. Thus, the replacement of part of the cement with secondary by-products such as blast furnace slag (BFS) and coal fly ash (FA) in blended cements can reduce the environmental impact [5,6]. However, in blended cements, the level of clinker replacement is usually no more than 35%, because the initial mechanical strengths would be seriously affected above this value.

Alkali-activated materials (AAM) are considered a good alternative to the traditional PC-based systems, showing high mechanical performance, equal to or even better than traditional PC [7–9]. AAM require strong alkaline activators such as NaOH [10] or sodium silicate (waterglass) solutions [11] to generate adequate compact cementitious materials [12–14]. Those materials, depending on the type of precursor (poor in Ca, such as FA or metakaolin, or rich in Ca, such as BFS), generate basically two different types of gels: a C-A-S-H gel (produced in Ca-rich systems such as alkali activated slag, AAS) [15,16] and a N-A-S-H gel, when Ca-poor precursors are

* Corresponding author.
E-mail address: sshagnay@ing.uc3m.es (S. Shagñay).

https://doi.org/10.1016/j.jobe.2022.105733
Received 22 September 2022; Received in revised form 1 December 2022; Accepted 11 December 2022
Available online 12 December 2022

employed [17,18]. The alkaline activators used to produce AAM, usually concentrated solutions of NaOH and Na_2SiO_3, produce a significant environmental impact [19], and their handling is complicated due to their very high pH values and corrosive nature.

Hybrid cements (HC) have emerged as an alternative to this problem. Several researchers [20–23] have determined that mixing a high content (70–80 wt%) of supplementary cementitious materials (SCM) such as BFS or FA with relative low proportions of PC (20–30 wt%) produces materials with good properties [24,25], and does not even require a high content of activators. HC are of great interest due to their good behaviour, which is attributed to the precipitation of a mixture of gels, with (C,N)-A-S-H or N-(C)-A-S-H being the main reaction products [23]. Based on previous studies on these hybrid systems [24,26], it has been possible to verify that slag-based hybrid cements (HS) have presented the best results in terms of durability, due to the formation of a more cohesive C-A-S-H gel than FA hybrid cements. That is why this work has focused on HS [24].

One of the main issues for the durability of PC-based concrete is the decalcification of materials [27,28], due to the leaching of calcium from the pore solution of the cementitious matrix to the environment. Aggregates can also been leached [29]. This phenomenon typically affects structures in contact with pure and acidic waters for long periods: dams, water pipes, radioactive waste disposal facilities, etc. [30].

Decalcification phenomena can generate mineralogical and microstructural modifications of the phases comprised in the pastes. Many research studies [31–33] have demonstrated that, in PC, the hydrated cement phases dissolve during leaching, releasing Ca^{2+} ions from either portlandite (CH) and C–S–H gel. Portlandite dissolution in the environment takes place first, and the decalcification of C–S–H occurs later [34]. The portlandite dissolution causes an increase of the pore network in the material, while C–S–H decalcification leads to binders with lower Ca/Si ratio, a more porous and heterogeneous structure [35]. Moreover, ettringite ($Ca_6[Al(OH)_6]_2(SO_4)_3{\cdot}26H_2O$) and anhydrous cement paste, when present in the binder, also suffers decalcification [28,36]. However, ettringite is more leaching-resistant than other phases resulting from clinker hydration [31].

Leaching fosters the development of a multilayer modified structure around the bulk material [37]. The critical consequence of the microstructural reactions occurring during decalcification is the increase in the porosity, which reduces the mechanical properties of the structural material [29,34,38] and increases its permeability [33].

According to literature, immersion in NH_4NO_3 fosters the decalcification process in cementitious materials [35,38–40]. Ammonium nitrate is very soluble in water and reacts easily with cement pastes, accelerating the leaching process [41]. The NH_4^+ ion reacts with OH^- ion from portlandite or other dissolved hydroxides comprised in the pore solution, forming ammonia, while the nitrate reacts with the Ca^{2+} precipitating as calcium nitrate and favouring the dissolution of solid Ca-containing phases present in the binder.

The Ca-leaching equilibrium curve in 6 M NH_4NO_3 has a similar shape to that obtained in water, which suggests a dissolving and leaching mechanism similar to water [42]. However, the Ca-lixiviated amount is about two orders of magnitude higher in NH_4NO_3 than in water [42]. In the equilibrium curve, three stages can be distinguished: (a) the first one, corresponding to the quick CH dissolution and lixiviation process; (b) the second one, where the slow decalcification of C–S–H gel takes place; and (c) the third one, where C–S–H gel with a Ca/Si ratio lower than 0.5 is quickly and totally decalcified [42].

The rate of this process can be affected by the degradation taking place in aggregate-binder interface [38,43], but, obviously, the binder composition (amount and nature of phases present) is also a key point [35,40,44]. Although the accelerated decalcification for traditional PC occurs through a well understood mechanism [31–33,45], it has been demonstrated that pozzolanic additions to pure clinker cement decrease calcium leaching, due to the lower amount of CH present in those binders [40].

In the case of the AAM, there is still scarce research on their decalcification behaviour. Park et al. [46] studied their electrically accelerated leaching, and demonstrated that Ca-rich AAM manufactured from slag suffer more leaching than FA-based activated materials (AAF) that comprised less calcium. AAS presented higher decalcification than AAF due to hydration of anhydrous slag and due to lower hydraulic reactivity of FA and the higher energy for N-A-S-H gel activation. Finally, as far as we know, there are no studies regarding decalcification for HC systems.

This study, based on accelerated leaching in an aggressive solution (NH_4NO_3), offers new data to evaluate the durability of the cementitious materials against the attack of soft or acid waters. The aim of the present work is to explore the decalcification resistance and mechanism for eco-efficient cementitious materials, such as AAM and HC pastes manufactured from BFS slag and compare them to a PC-based system (CEM IV/(B) Q 32.5 R). Novelty relies on the study of leaching of hybrid materials and deepening in the knowledge of leaching process of alkali activated materials, where literature is very scarce.

2. Materials and experimental procedure

2.1. Materials

Two types of PC (CEM I 52.5 R and CEM IV/B (Q) 32.5 R, provided by Cementos Portland Valderribas, Madrid, Spain) were used. The CEM IV, with high content in natural pozzolans and fly ash, according to UNE-EN 197-1 standard, was used as the reference commercial system, while CEM I was used for the preparation of the HC (80 wt% BFS + 20 wt% CEM I). BFS, provided by the Avilés factory in Asturias, Spain, was used as the precursor for both AAS and HS systems. The chemical composition of the raw materials, determined by X-ray fluorescence spectroscopy (XRF), is shown in Table 1. The AAS was activated with waterglass, using a commercial sodium silicate solution (Merck, 27% SiO_2; 8% Na_2O and 65% H_2O by weight) with a SiO_2/Na_2O ratio of 1.2. Solid Na_2SO_4 (powders) was added as soft alkaline activator in the HS system.

2.2. Preparation of the cementitious pastes

Table 2 shows the formulation of the different cementitious systems studied. PC (CEM IV) paste was hydrated exclusively with deionized water. As previously stated, AAS was activated with a waterglass dissolution (SiO_2/Na_2O = 1.2). The HS pastes were

Table 1
Chemical composition (wt%) of raw materials determined by XRF.

	CaO	SiO_2	Al_2O_3	MgO	Fe_2O_3	SO_3	K_2O	TiO_2	[a]L.O.I.
CEM I	61.0	20.9	6.3	< 0.01	2.5	5.8	1.0	0.2	2.3
CEM IV	30.1	43.4	11.7	1.5	4.8	3.0	1.2	0.4	3.5
BFS	37.4	34.3	11.4	11.7	0.2	1.9	0.3	0.5	2.1

[a] L.O.I. loss of ignition (1000 °C).

Table 2
Dosage of cementitious pastes and activation condition.

Name	Precursor	Wt. % of CEM I	Wt. % of CEM IV	Wt. % of BFS	Wt. % of solid activator	L/S	Hydration media
CEM IV	CEM IV	0	100	0	–	0.35	Water
AAS	BFS	0	0	100	–	0.50	Waterglass
HS	BFS + CEM I	17.5	0	77.5	5 (Na_2SO_4)	0.40	Water

supplemented with a moderate alkaline activator (5% wt. of Na_2SO_4 with respect to the blend). In the case of HS, the solids (precursors + activator) were pre-mixed in a turbula, and the system was consequently water hydrated. In HS materials, Na_2SO_4 was selected due to its good solubility. Moreover, Na_2SO_4 reacts with portlandite (Eq. (1)), generating a high alkalinity medium (high pH value, around pH = 13). This alkaline environment accelerates the dissolution of BFS and promotes the pozzolanic reaction.

$$Ca(OH)_2 + Na_2SO_4 \leftrightarrow CaSO_4{\cdot}2H_2O(s) + Na^+ OH^- (aq.) \quad (1)$$

The liquid/solid ratio (L/S) was chosen to obtain equal consistency for the different pastes, according to the criteria detailed in the UNE-EN 1015-3 standard.

Pastes were then poured into sealed cylindrical PVC moulds with 10-cm diameter and samples were subsequently cured in a chamber at 99% relative humidity and 21 ± 2 ºC for 28 days. After the curing, moulds of the PVC with pastes were segmented into 3-cm thick slices (Fig. 1). The free space between the PVC mould and the lateral of the pastes was sealed with an epoxy resin (ARALDITE® Rapido) to ensure that only top and bottom surfaces were exposed to the leaching solution [31,33].

Reference samples of the four types of pastes were manufactured in the same way as the ones to be subjected to the leaching test and kept in an empty and sealed desiccator (N_2 atmosphere) for 28 days (without contact with NH_4NO_3 solution). After that time, samples were characterized the same way as the NH_4NO_3 leached pastes.

2.3. Leaching test procedure

Two 3-cm thick samples of each system were immersed in a 6 M NH_4NO_3 solution. The solution volume/surface area ratio was 8 cm^3/cm^2 and the solution was continuously magnetic stirred to keep the solution homogeneous, as has been previously described in other publications [31]. After 0, 1, 7, 14, 21, 28 days of exposure, a small aliquot was extracted (5 mL) and its pH was monitored to ensure that the pH value remained below 9.25 [47].

The aliquot was analyzed with inductively coupled plasma optical emission spectroscopy (ICP-OES) to determine and quantify the calcium and other elements leached. Fig. 2 shows the set-up used for the tests, where the pipes connected to the desiccators allow the entrance of a constant flow of nitrogen to avoid carbonation [31], while the other extreme allows the removal of NH_3 generated during the test.

2.4. Characterization of the leached pastes

After 28 days of immersion, all samples were characterized by different techniques as follows. Immersed samples were cut perpendicular to the attacked surface (Fig. 3). Each transverse section was sprayed with phenolphthalein to determine the pH decrease

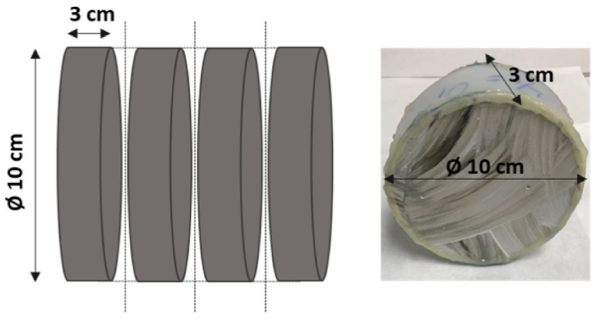

Fig. 1. Preparation of the samples after cutting segmentation into 3 cm thick layers.

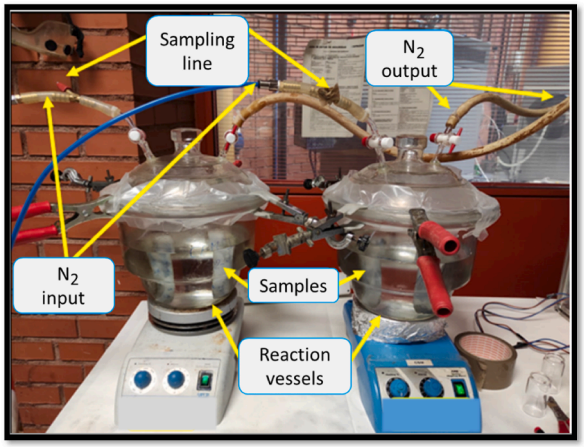

Fig. 2. Accelerated leaching test set-up.

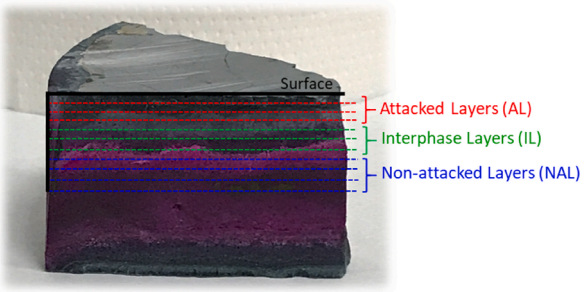

Fig. 3. Transverse section of the pastes sprayed with phenolphthalein after NH_4NO_3 exposure, showing the designation of different regions (attacked, interphase and non-attacked).

caused by leaching (Fig. 3). Three zones were determined in each specimen: the most external (leached zone), the intermediate zone, and the most internal, non-attacked (non-leached) zone. Samples were obtained from each zone, and those specimens were immersed in isopropanol for 2 days, and subsequently stored under vacuum in a desiccator for 7 days to eliminate all the liquid inside the samples [31,33]. Those samples were employed to analyze the changes that have taken place. A caliper was used to measure the different depths of zones defined after the tests [48].

Moreover, a summary of the selected samples is detailed in Table 3. The different layers are identified by "AL", "IL" or "NAL" (depending on the selected region, "attacked layer", "interphase layer" and "non-attacked layer" respectively). Slices were cut from the leached zone to the non-leached one. The depth from the external surface to each layer is also indicated in Table 3.

Prismatic samples measuring approximately 1 cm^3 were taken from both the outer leached zone (AL) and unaltered inner zone (NAL). Different zones were distinguished from transversal sections after spraying them with phenolphthalein (Fig. 3). Changes in its microstructure were explored with mercury intrusion porosimetry (MIP) and backscattering electron microscopy with energy dispersive X-ray spectroscopy analysis (BSEM/EDX). MIP measurements were performed to determine the total volume of open porosity and the pore size distribution with a Micromeritics AutoPore IV 9500 analyzer, able to exert pressures from 0.5 up to 33000 psi. Samples obtained from AL and NAL zones were embedded in epoxy resin for BSEM/EDX studies. The observation was carried out with a JOEL JSM 6400 equipment under BSE mode at 20.0 kV, and fitting resorts to an integrated Link ISIS EDX analyzer.

Monolithic specimens were sliced into thin layers (Table 3) to obtain representative slices of AL, IL and NAL regions (Fig. 3). A high precision cutting machine was used for obtaining the slices. It was operated at the minimum speed to minimize damage to the material during the process. Each layer was ground into a fine powder and mixed in a breaker with isopropanol to detain hydration.

Table 3
Designation of different areas under study.

CEM IV	**Layer**	[a]**AL1**	[a]**AL2**	**AL3**	**AL4**	[a]**IL5**	[a]**NAL6**	**NAL7**			
	Depth (mm)	1.95	3.39	5.14	6.84	8.59	10.60	11.48	–	–	–
AAS	Layer	[a]**AL1**	[a]**AL2**	**AL3**	**IL4**	[a]**IL5**	**IL6**	**IL7**	**NAL8**	**NAL9**	[a]**NAL10**
	Depth (mm)	1.5	3.84	6.01	8.18	10.35	12.52	14.72	16.97	19.06	21.23
HS	Layer	[a]**AL1**	[a]**AL2**	**AL3**	**IL4**	[a]**IL5**	**IL6**	**NAL7**	**NAL8**	**NAL9**	[a]**NAL10**
	Depth (mm)	1.5	4.34	6.51	8.58	10.85	13.02	15.19	17.36	19.53	21.70

[a] Selected layers for further XRD, FTIR and TG studies.

The powder was stirred in isopropanol for 1 min filtered by 4 min through a 0.45 μm polyamide membrane filter and dried in an inter atmosphere desiccator at 20 °C. Mineralogical and compositional changes, in powder of each layer obtained from samples indicated in Table 3 were analyzed by X-ray diffraction (XRD), thermogravimetry (TG), and Fourier-transform infrared spectroscopy (FTIR). XRD of powder was analyzed by a Philips CuK radiation PW 1730 diffractometer. Each scan was measured from 2° to 60°, step size was at 0.02°, using a 0.5° divergence slit, and time/step was 1 s. TG was conducted by a Q600 TA SDT analyzer in Al crucibles (reference, empty crucible) with experimental conditions of 25 °C to 1050 °C in a N_2 atmosphere flowing at a rate 20 L/min. FTIR was developed by an ATIMATTSON FTIR-TM series spectrophotometer. Spectra analysis was performed at a resolution of 4 cm^{-1} over a range of 4000 cm^{-1} to 400 cm^{-1}.

3. Results and discussion

3.1. Lixiviation of ions and pH decrease

To obtain information about the changes that took place in the different pastes exposed to accelerated leaching in NH_4NO_3, phenolphthalein was used to determine the decalcification depth. Images of the CEM IV, AAS and HS samples without being immersed in the solution can be seen in Fig. 4a and c and **4e.** For these samples, phenolphthalein is not able to show any pH decrease through the thickness of the pastes after 28 days. Fig. 4b, d and **4f** show the leaching penetration of the three materials after being immersed in the NH_4NO_3 solution for 28 days. It is worthy of note that the leaching depth was slightly deeper for CEM IV than for AAS and HS. For CEM IV, a colorless region of approximately 8.7 mm was determined, while it was 5.8 mm and 6.6 mm in AAS and HS, respectively. Bearing in mind that this pH indicator (phenolphthalein) changes from purple to colorless between 10 and 8.2, a pH lower than 10 can be clearly assigned to the "attacked" regions.

The CEM IV, in spite of its high amount of pozzolanic additions and smaller alkaline reserve than other commercial cements with higher clinker content, is the material with highest alkaline reserve among those studied, due to its portlandite content. Previous studies have verified that after 28 days of curing CEM IV materials have much higher porosity than AAS [26] and HS [24]. So, the fact that it has the lowest ability to keep high alkalinity inside the pores of the bulk material can probably be related to a higher volume of interconnected porosity that would favor OH^- lixiviation [33].

Results regarding the chemical changes due to the progress of the test in the lixiviating solution are plotted in Fig. 5 for the different pastes. As can be seen, the pH increases quickly during the beginning of the test, changing from values typical of a weak acidic solution to characteristic values of solutions with weak alkalinity. This rapid increase can be identified with the diffusion of the soluble hydroxides present in the different pore solutions. Na^+ and K^+ are highly soluble and quickly diffuse to the testing solution to balance their concentrations, so both alkaline ions reach their limit value in solution before a week. As expected, after checking the chemical composition of the materials (Tables 1 and 2), K^+ is found in CEM IV and materials manufactured with BFS, while Na^+ is found in the lixiviation of materials activated with compounds containing this element. Ca^{2+} also quickly increases its concentration in the lixivi-

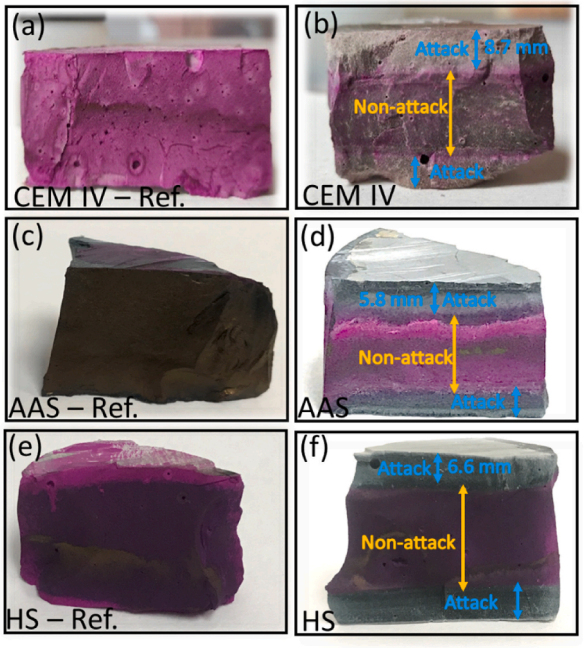

Fig. 4. Visual appearance of the materials evaluated after phenolphthalein spraying. **a)** CEM IV reference, **b)** CEM IV leached, **c)** AAS reference, **d)** AAS leached, **e)** HS reference, **f)** HS leached.

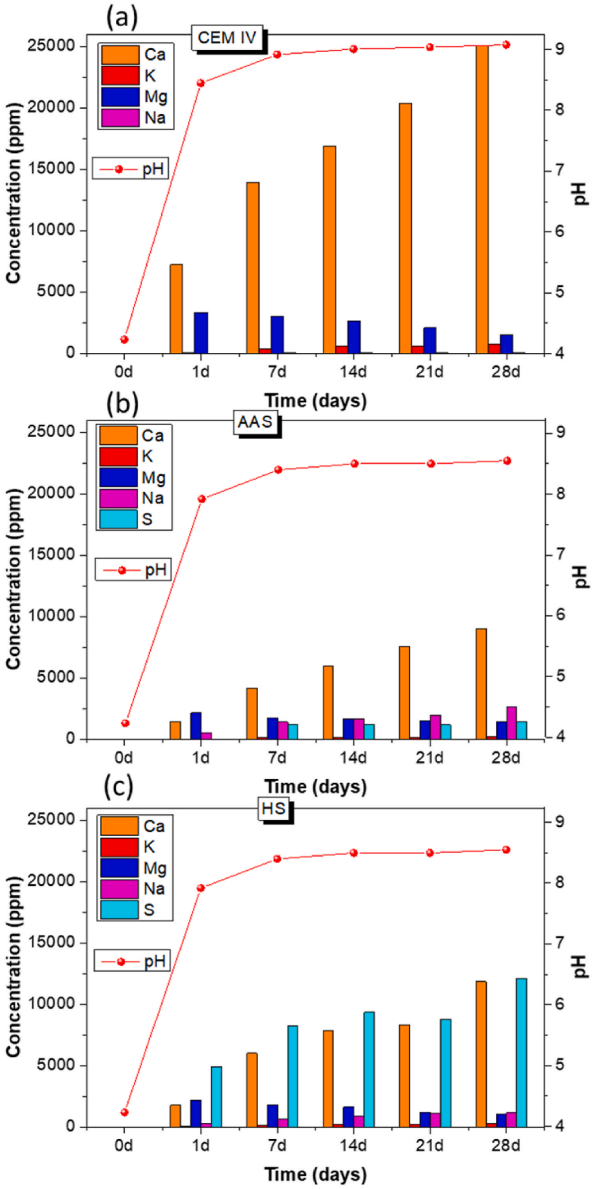

Fig. 5. Change during exposure time of concentrations of the elements leached from the pastes to the NH_4NO_3 solution and pH values of the solution.

ating solution. This calcium can be originated from portlandite dissolution (Eq. (2)), from ettringite dissolution (Eq. (3)), from C–S–H gel (Eq. (4)), or from carbonate phases, among others, after the attack with the solution of NH_4NO_3.

$$Ca(OH)_2 + 2\,NH_4NO_3 \leftrightarrow Ca^{2+} + 2\,NO_3^- + 2\,NH_3\uparrow + 2\,H_2O \quad (2)$$

$$6\,H^+ + 3CaO{\cdot}3CaSO_4{\cdot}Al_2O_3{\cdot}32H_2O + NH_4NO_3 \leftrightarrow 6\,Ca^{2+} + NO_3^- + 3\,SO_4^{2-} + 2Al(OH)_3 + NH_4^+ + 32\,H_2O \quad (3)$$

$$(CaO)_x(SiO_2)_y(H_2O)_z + 2wNH_4NO_3 \leftrightarrow (CaO)_{(x-w)}(SiO_2)_y(H_2O)_{(z-w)} + w\,Ca^{2+} + 2wNO_3^- + 2w\,NH_3\uparrow + 2w\,H_2O \quad (4)$$

The Ca^{2+} measured in the lixiviating solution is clearly highest for CEM IV, although crossing the data of Table 1 and **2,** it can be easily checked that it is not the binder with the highest CaO content: 30.1% of CaO in CEM IV versus 37% comprised in AAS or 42% in HS. Hence, it is clear that for the Ca^{2+} lixiviation processes, the key point is not the amount of calcium present in the matrix, but its hydrated form after curing. If the calcium leaching is compared between AAS and HS, it is observed that HS systems have higher calcium leaching, and could be due to the fact that the HS pastes were manufactured with a small percentage of CEM I and their composition contained more calcium.

Moreover, magnesium is present in all the materials (Table 1) and is comprised in solid phases of the hydrated binders is Mg^{2+} [49]. This ion is quickly lixiviated during the first hours of the test and then its concentrations tend to decrease. This is probably due to fact that, as the pH of the solution increases, the lixiviating Mg^{2+} becomes insoluble and precipitates as $Mg(OH)_2$. Hence, an increase in concentration of this ion is not seen over time.

Ions such as aluminium or iron, present in the raw materials (Table 1), do not appear in the leaching solution. This could be related to the stability of the solid forms of these elements at moderately alkaline pHs. The absence of aluminium in the leaching solution has also been pointed out by other authors studying the performance of CEM I pastes [31].

Regarding the leached sulfur content, it is important to note that both the AAS and HS systems show a high content of this element in the solution after the attack with the NH_4NO_3 solution. This leached sulfur comes mainly from the activator used in the HS system (5% Na_2SO_4). Possibly what is happening is that the Na_2SO_4 has not completely dissolved during the activation process or that the dissolution of NH_4NO_3 is attacking any secondary phase formed. Being a hybrid system, the presence of portlandite is due to the PC hydration, which should react with sodium sulfate (highly soluble) to generate NaOH and hydrated $CaSO_4$ (see **Eq. (1)**), so this $CaSO_4{\cdot}2H_2O$ is being attacked by the leaching solution [50]. In AAS, the high S content of CEM I (Table 1) can explain the observed leached data.

Leaching data were also compared with the increase in pH of the solution. This pH is related to the leaching rate. In all cases, pH greatly increased in the first week, due to the rapid lixiviation of the alkalis present in all systems. After this, their values continued to increase, but at a slower rate, due to the leaching of the innermost layers as the C–S–H gel decomposes. The behaviour, in terms of evolution of the pH values, was similar for all systems.

Moreover, Fig. 6 shows Ca^{2+} concentration in the leaching dissolution against the square root of the immersion time, that is the kinetic expected for a purely diffusion-controlled process. The diffusion rates for Ca^{2+} in CEM IV are much faster than in AAS and HS. In this material, the higher amount of more easily leachable calcium makes the rate of the diffusion process (related to slope of the fitting) the fastest.

3.2. Microstructural changes

The total porosity and pore size distribution for all the pastes after the 28 days of immersion in NH_4NO_3 are represented in Fig. 7. The porosity and pore size analysis were conducted in both the leached zone (labelled as “attack” in Fig. 4) and un-leached zone (labelled as “non-attack”). The porosity of reference samples is represented.

The results show that the total porosities and pore size distribution (see Fig. 7) of CEM IV and HS references are quite similar. Comparing these results with the porosity volume of as-cured materials at 28 days [24], it is clear that the hydration processes have continued in CEM IV in a marked way, and its porosity has been reduced to become similar to that of HS mortars.

However, when the attack by the ammonium nitrate solution occurs, there is a significant increase in porosity, approximately 45%, for both CEM IV and HS systems. In CEM IV, it is due to the leaching of calcium from the portlandite and C–S–H gel, causing greater cracking in the system. For the HS system, porosity in the attacked area is slightly higher, not only due to calcium leaching, but also to sulfur leaching. The presence of sulfur causes new phases to be formed after the reaction with the portlandite, like $CaSO_4{\cdot}2H_2O$ (see **Eq. (1)**), with its leaching taking place and, therefore, generating porosity. Finally, the porosities of the CEM IV and HS systems in the non-attacked zones are very similar to the initial ones, although there is a slight increase in the total porosity.

On the contrary, attacked AAS presents the lowest total porosity, being approximately 50% lower than the two previous systems. A major change occurs in pore size ratio, with the amount of pores below 0.1 μm increasing (Fig. 7c). Previous work [14] has showed that AAS, due to their C-A-S-H gel content, exhibit high stiffness and hardness. In addition, the pores of the gel formed in these systems are smaller than 0.01 μm, as a consequence of the sodium silicate addition, which greatly reduces the pores above 10 μm and the capillary pores (between 0.01 and 10 μm) [31].

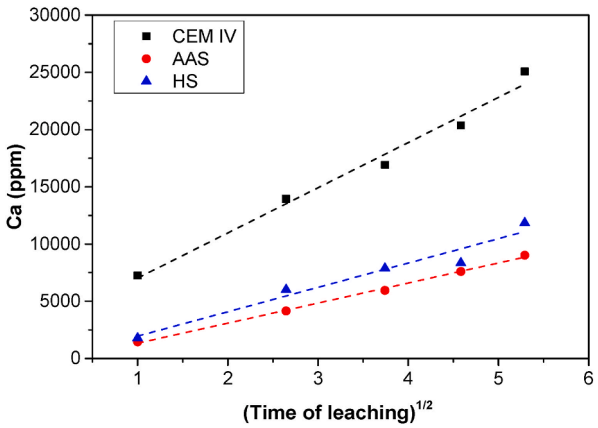

Fig. 6. Variation in calcium leached over time.

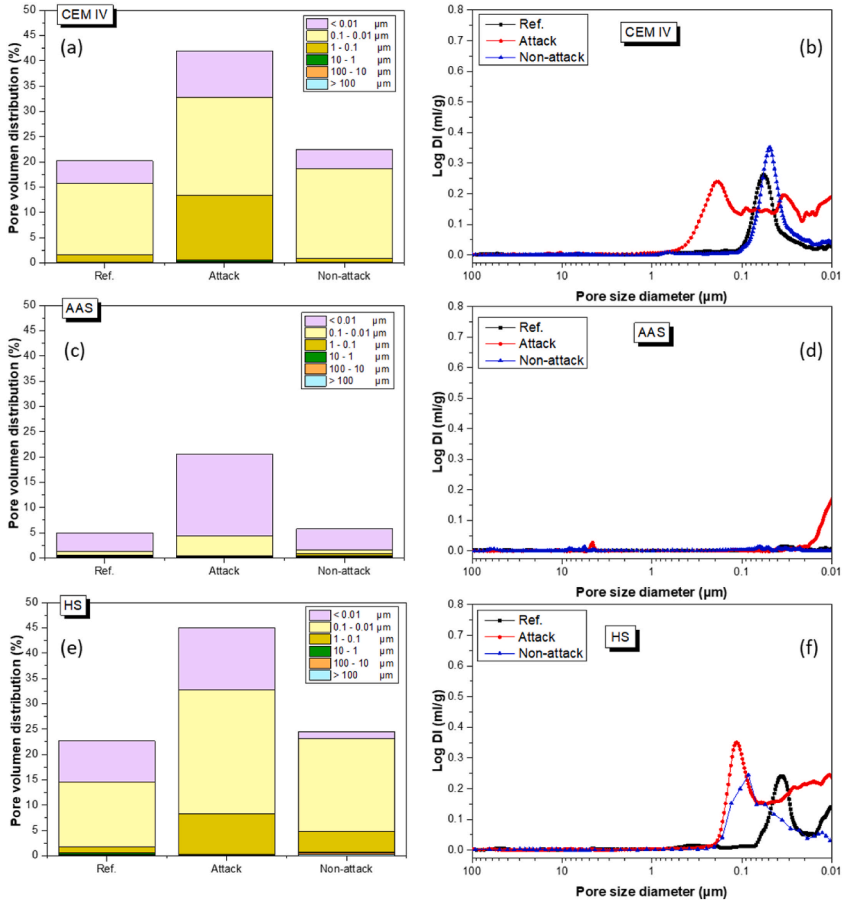

Fig. 7. Pore volume (%) and pore size distribution of (a) CEM IV, (c) AAS, (e) HS. MIP Hg intrusion log differential vs pore size of (b) CEM IV, (d) AAS, and (f) HS.

At the same time, the attacked zone always has higher porosity than the non-attacked zone and the reference material. In all materials, porosity of non-attacked zones is half that of the attacked ones. Ultimately, Hg intrusion data confirm that the pore size distribution is higher for all systems in the attacked zone.

Fig. 8 shows the BSE micrographs of the CEM IV, AAS and HS systems that were in direct contact with the NH_4NO_3 solution, displaying images of the areas that suffered attack and of those that did not suffer calcium leaching. As can be seen in the micrographs, the leaching process in all systems greatly affected the microstructure of the samples. In the non-attacked zone, a more compact matrix and homogeneous distribution of the different phases are observed. However, in the attacked zone, it is easier to detect a less robust microstructure. As has been pointed out before, the leaching phenomenon for CEM IV systems causes an alteration of portlandite, C-A-S-H gel and the anhydrous clinker particles (C_2S, C_3S) or $CaCO_3$ particles, among others, thus generating empty edges [31].

The presence of unreacted (anhydrous) BFS particles can be clearly observed in the CEM IV pastes (Fig. 8a). The presence of anhydrous FA particles (in the form of spheres) was also observed, although to a lesser extent. As the leaching front advances (attacked zone), a morphological change is observed, where a better distinction between the phases present, both anhydrous and those formed during cement hydration, can be seen.

For the AAS system, the entire surface shows cracks and micro-cracks due to the common shrinkage that is generated in this type of binders [51–53], while larger cracks can be observed in the attacked zones. Likewise, HS systems show a difference between the attacked and non-attacked zone; the non-attacked regions have a visually compact microstructure, while the attacked zone has uncompacted microstructure and considerable loss of material on the surface (see Fig. 8c). Moreover, micropores can be clearly seen in the attacked region (Fig. 7e).

EDX is a widely applied elemental microanalysis method capable of identifying and quantifying (semi-quantification) elements. It was used to determine the elemental distribution and elemental maps (see Fig. 9) confirm the different elements present in both zones (attacked and non-attacked) for each system evaluated. As expected, the calcium concentration in the attacked zone is much lower than in the not-attacked zone. Thus, EDX corroborates the change from the initial Ca-rich composition to a Si-rich one in the attacked zone of CEM IV. Moreover, for AAS and HS, there is a considerable loss of Na and S in the attacked zone, as previously mentioned in the ICP-AES leaching results (Fig. 5). In addition, the calcium content decreases considerably in the AAS and HS systems (see Fig. 10), indicating that the NH_4NO_3 attacks the calcium present in the system. This calcium leached from base material comes from the decal-

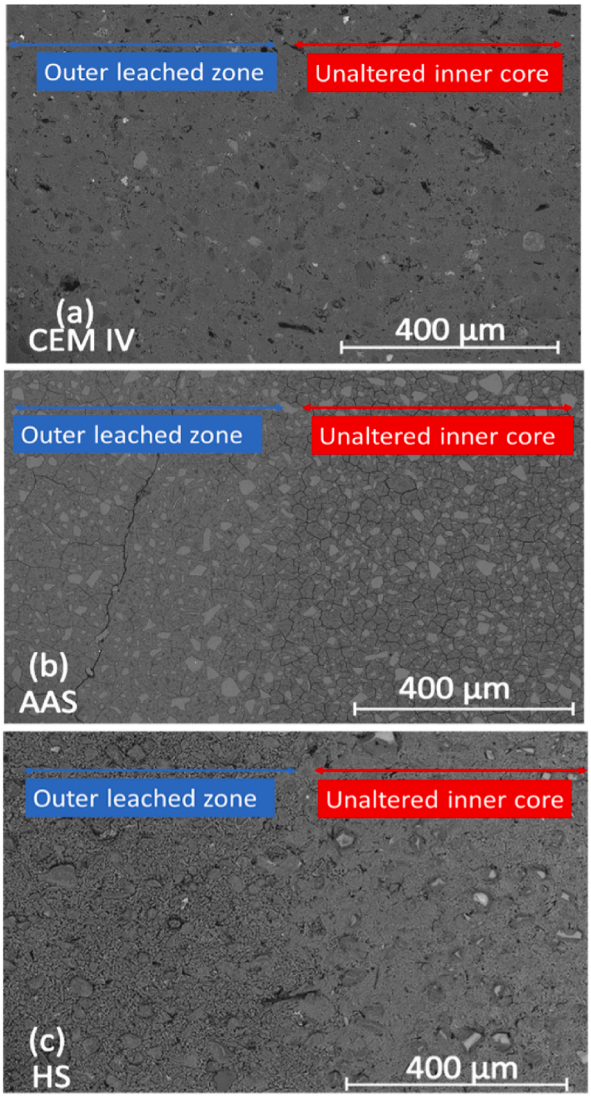

Fig. 8. BSE micrographs of the interphase region of: **(a)** CEM IV, **(b)** AAS, **(c)** HS exposed to NH_4NO_3 dissolution.

cification process of the main hydration product (C-A-S-H gel). In this way, as can be seen in the ternary diagrams, in the AAS system, initially a Ca/Si = 1.3 ratio is found. This ratio is slightly high due to the possible carbonation of the sample, since these systems originally have a Ca/Si ratio around 0.9–1.2 [11]. However, it is observed that, after the leaching process, this Ca/Si ratio decreases considerably to values of Ca/Si = 0.2. It would not be a pure silica gel because magnesium is present in the system. On the other hand, regarding the HS sample, initially it has a Ca/Si = 1.9 ratio and after the leaching process a Ca/Si ratio ≈1.0 is obtained. By way of comparison between both systems, the loss of calcium after the leaching process is clearly observed. It is important to highlight that this quantification is performed using a semiquantitative technique (SEM-EDX).

3.3. Mineralogical and structural changes in the pastes

Fig. 11 shows the different diffractograms evaluated for all systems after 28-days immersion in the NH_4NO_3 solution and for each of the studied layers (attacked and non-attacked zones). The reference system has also been added. Fig. 11a shows the XRD patterns corresponding to the CEM IV system. No significant mineralogical differences were found in the non-attacked layers (NAL6). In these non-attacked layers, typical hydration products of Portland cement [31] were observed, such as portlandite, ettringite, and AFm phases. Moreover, due to the presence of FA in this CEM IV, the presence of mullite and quartz in the XRD pattern is evident.

As the leaching front advances through the specimen, differences are observed. In the diffractogram of the CEM IV system (Fig. 11a), the so-called attacked layers (AL1, AL2) do not contain reflexes associated with the presence of portlandite. All of these facts are significant and reveals that the calcium present both in the portlandite and in the different calcium silicates are the first ones leached. The reaction produced between the portlandite and the ammonium nitrate solution, causing the disappearance of the portlandite, is

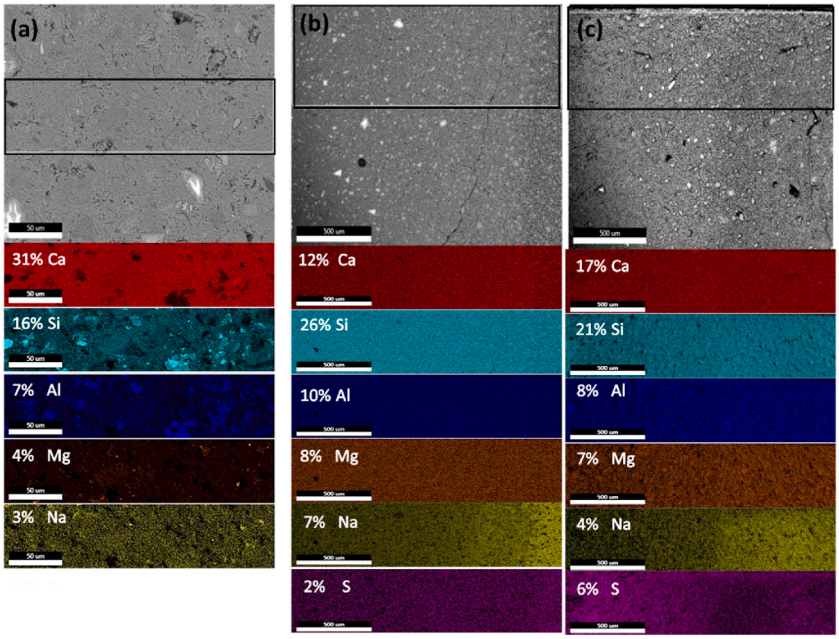

Fig. 9. EDX mapping of the interphase region: **(a)** CEM IV, **(b)** AAS, **(c)** HS, exposed to NH_4NO_3 solution.

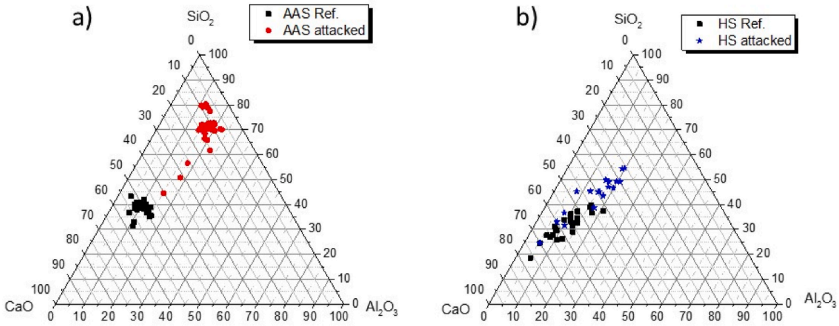

Fig. 10. Ternary diagrams with the chemical composition of the main reaction products formed (C-A-S-H gel) in the different systems evaluated before and after the leaching process **a)** AAS and **b)** HS.

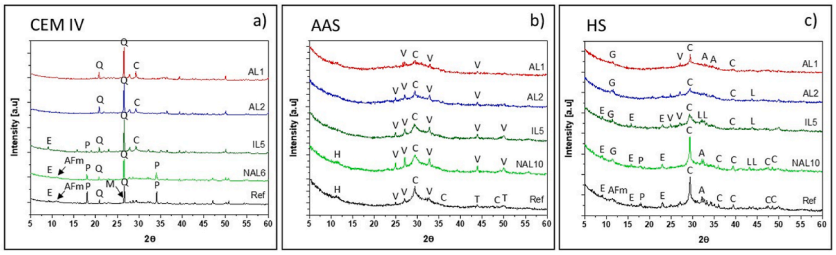

Fig. 11. XRD patterns for: **a)** CEM IV, **b)** AAS, **c)** HS. (Legend: Q-quartz (COD: 2300370); E–ettringite (COD: 9015084); AFm (COD:PDF 41–0221); P-Portlandite (COD:1529752); M-Mullite (COD:9001621); H-hydrotalcite (COD: 9009272); V-vaterite (COD: 9007475); C-calcite (COD: 9009667); T-tobermorite (COD: 9002245); A-Alite (COD: 1540705); L-larnite (COD: 9012790); G-Gypsum.

governed by Eq. (2) [31]. Portlandite dissolves faster than other calcium compounds comprised in the binders. The alkaline pHs existing in the pore solution at the beginning of the test (Fig. 5), is due to the chemical reaction proposed in Eq. (2). The continuous evolving of gaseous ammonia in this process, as it is purged from the system, facilitates the shift of the reaction to the products and the development of an accelerated test. The proposed reaction has also taken into account the high solubility of the calcium nitrate that allows the dissolution and lixiviation of Ca^{2+} ions. When portlandite is dissolved, the dissolution of other phases present starts. The C–S–H decalcification in a moderately alkaline pH, as the one expected, must follow the reaction shown in Eq. (4). For the proposal of this reaction, it has been borne in mind that alumina is clearly stable at pHs lower than 9, that is to say, similar to those determined in

the testing solution after a few days, and that must also exist in the pore solution after the hydroxides have already been dissolved (Fig. 5).

Moreover, it is also observed that in the attacked layers the reflexes belonging to ettringite and AFm phases, like monocarboaluminate hydrate, disappear. The ettringite dissolution in NH_4NO_3, which also takes place slowly at moderately alkaline pHs [42], is proposed to follow **Eq. (3).**

The AAS diffractogram (see Fig. 11b) shows significant changes between the attacked (AL1 and AL2) and non-attacked (NAL10) layers. The main products of this material are identified, such as calcite or hydrotalcite, among others [54–56]. Moreover, it can be observed that the reflexes belonging to calcite ($2\theta = 29.4°$), hydrotalcite ($2\theta = 10.8°$), and merwinite ($2\theta = 50°$) disappear in the surface layer (AL1), due to its greater contact with the NH_4NO_3 solution [56]. Hydrotalcite would have a decomposition reaction with ammonium nitrate as follows (**Eq. (5)**):

$$Mg_6Al_2CO_3(OH)_{16}{\cdot}4H_2O + NH_4NO_3 \leftrightarrow 6\ Mg^{2+} + NO_3^- + HCO_3^- + 2\ Al(OH)_3 + 4\ H_2O + \uparrow NH_3 + 10\ OH^- \quad (5)$$

In addition, Fig. 11c shows diffractograms for HS system, where it can be clearly seen that the reflexes belong to portlandite ($Ca(OH)_2$) and ettringite ($Ca_6Al_2(SO_4)_3(OH)_{12}{\cdot}26H_2O$) in reference material and the non-attacked layers (NAL10). The existence of portlandite and ettringite can be explained due to the presence of 20% (wt) CEM I in raw material (Table 2). Furthermore, the presence of calcite can also be observed as intense reflexes in the non-attacked layer (NAL10) diffractogram. While the attack progresses, its reflexes decrease and in the last attacked layer (AL1), the calcite disappears. In addition, the presence of minority phases of monocarboaluminate (AFm phase) in the non-attacked samples is observed, as well as the formation of gypsum ($CaSO_4{\cdot}2H_2O$) after the reaction of the portlandite with the sodium sulfate (used in this system as activator).

By XRD, it is complicated to observe an evolution of the main hydration product (C–S–H or C-A-S-H gel), since they are semi-crystalline compounds, which make them difficult to detect. For this reason, other complementary techniques will be used to provide more information, such as infrared spectroscopy (FTIR). However, it is known that a reaction is also taking place between the NH_4NO_3 solution with the calcium present in the main reaction product (C-A-S-H gel), as indicated in **Eq. (6)** [57]. The disappearance of the ettringite phase in the outermost layer can also be observed, producing the reaction according to **Eq. (3)** [57].

$$(CaO)_x(SiO_2)_y(H_2O)_z + 2w\ NH_4NO_3 + 2w\ H^+ \leftrightarrow (CaO)_{(x\text{-}w)}(SiO_2)_y(H_2O)_{(z\text{-}w)} + w\ Ca^{2+} + 2w\ NO_3^- + 2w\ NH_4^+ + 2w\ H_2O \quad (6)$$

XRD results show a similar behaviour for all of systems: there is always a reaction between the NH_4NO_3 solution and the portlandite, producing the decalcification of the later. Another important fact to highlight is the disappearance of ettringite in attacked layers (AL1 and AL2) of all systems. Both layers are the outermost ones, so they are the ones that were most in contact with the leaching solution.

TG curves (and their derivatives, DTG) for attacked, non-attacked layers and reference materials are shown in Fig. 12. For CEM IV, in all cases the peak found at 105 °C on the DTG curves (Fig. 12b) is related to the evaporation of free water as well as the water associated to hydrated phases such as ettringite and C–S–H gel. The same behaviour has been previously reported for CEM I by Garcia-Lodeiro [31], and it is also observed that the less intense peak is closer to the surface (NAL6) due to the loss of ettringite in the attacked zone. A second peak is clearly observed at 151 °C for the attacked layer (AL1 and AL2), which corresponds to the decomposition of the AFm phase. This peak disappears due to the leaching, while in the interphase (IL5) a small band is observed and in the non-attacked layer (NAL6). For the reference material, this peak is more intense. The peak at 445 °C was associated with dehydroxilation of $Ca(OH)_2$. It is more intense for the reference material and the non-attacked layer (NAL6) than for the attacked layers, indicating that more portlandite is comprised in the non-attacked layers and reference material. If a quantification of the region between 380 and 500 °C is performed for the REF and NAL6 layers, portlandite percentages of 10.47% and 9.42%, respectively, are obtained. This fact justifies the presence of portlandite in both layers, but an attack by ammonium nitrate is already being observed, making it difficult to quantify the presence of portlandite in layers IL5, AL2 and AL1. Furthermore, the peak at 720 °C belongs to decarbonation of $CaCO_3$.

On the other hand, in the AAS pastes (Fig. 12c and **d**), normally, the first stage (peak at 150 °C) is the loss of the water absorbed by the system or the interlayer water of C–A–S–H [58–60]. Moreover, the stage from 200 to 600 °C was associated to decomposition (loss of OH process) of the gel phases such as C–S–H or C–(A)–S–H [60], which could be seen in the non-attacked layer (NAL10). The intensity of the signal associated with the first peak was much lower in the attacked layers (AL1 and AL2, see Fig. 12d) than in the non-attacked layer (NAL10), denoting considerable difference in the percentage of water in the interlayer where the layers closer to the leaching agent would be most susceptible to decalcification. However, the attacked layers (AL1 and AL2) show a peak at 660 °C that was associated to decomposition of calcium carbonate [61]. Moreover, a peak at 400 °C can be seen (Fig. 12d), belonging to hydrotalcite decomposition, which clearly disappears in the attacked layers.

Fig. 12f shows different peaks related with HS. The first peak at 105 °C, observed for all the curves, is associated with the loss of unbound water and water in the hydrated phases such as ettringite, C–S–H or C–(A)–S–H gels due to the presence of 20% (wt) CEM I [61]. In the same way as in CEM IV (Fig. 12b), the HS peak at 151 °C was associated to decomposition of possible gypsum ($CaSO_4{\cdot}2H_2O$) and monocarboaluminate [62]. In this case, it is the reaction between Na_2SO_4 with portlandite to form NaOH and $CaSO_4{\cdot}2H_2O$, according to different studies [31,63]. Thus, $CaSO_4{\cdot}2H_2O$ in the presence of NH_4NO_3 decomposes (**Eq. (7)**). The solubility of $(NH_4)_2SO_4$ is much higher than that of $CaSO_4{\cdot}2H_2O$, so the high sulfur content observed by ICP-AES (see Fig. 5c) can be attributed to the formation of this salt.

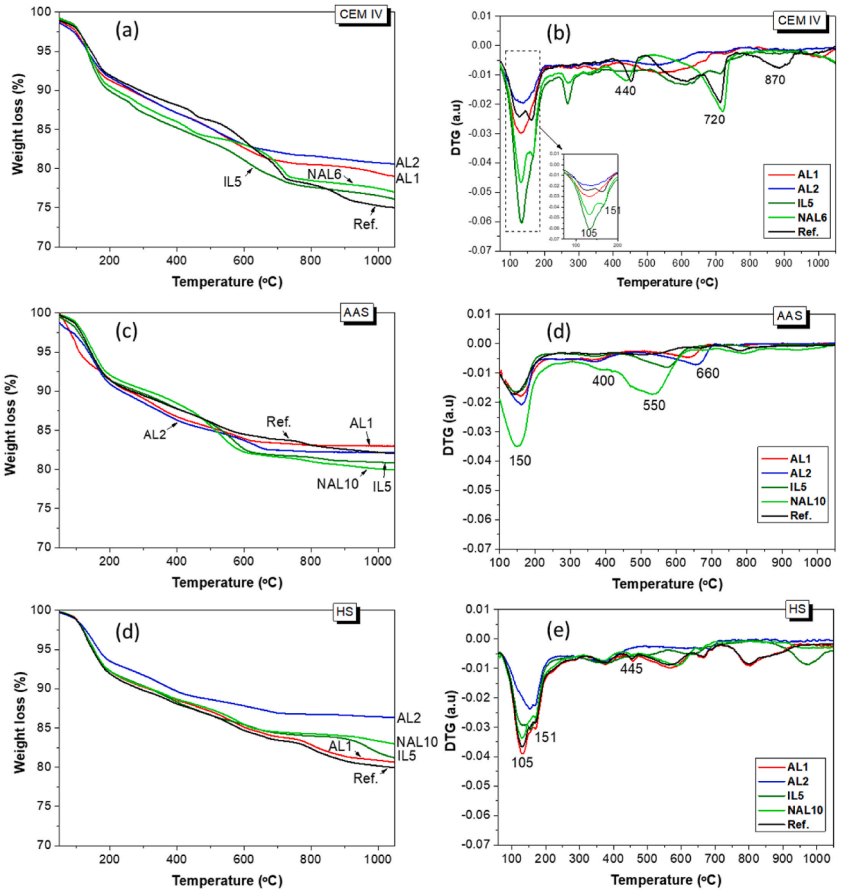

Fig. 12. TG and DTG curves for attacked, interphase, non-attacked layers and reference of each system: **(a,b)** CEM IV, **(c, d)** AAS, and **(e, f)** HS.

$$CaSO_4{\cdot}2H_2O + 2\,NH_4NO_3 \leftrightarrow (NH_4)_2SO_4 + Ca(NO_3)_2 + 2H_2O \quad (7)$$

In addition, the reference material shows a peak at 445 °C that was associated to dehydroxylation of portlandite. In the same way as with the CEM IV system, a quantification of portlandite can be made in the region between 430 and 480 °C. 2.59% portlandite is present in the HS reference layer being practically non-existent. This fact can already be verified by XRD, with a slight presence of portlandite in the reference layer and somewhat in the NAL10 layer (see Fig. 11). The peak in range 500 °C–600 °C that is present for all the materials could be related to the dehydroxylation process of the different phases as C–S–H or C–(A)–S–H, as mentioned previously for AAS. The peak at around 800 °C corresponds with the decomposition of calcite, while the signal around 859 °C was attributed to the loss of the hydroxyl groups in C–S–H gel, as it is converted to wollastonite [64]. It should be noted that this signal is especially significant in the case of the reference sample and in the NAL10, indicating that the amount of C–S–H/C-(A)-S-H gel is higher in the non-attacked samples. The disappearance of this signal in the attacked areas is a clear indication that the C–S–H/C-(A)-S-H gel is being decomposed in contact with the ammonium nitrate solution.

Fig. 13 shows the different infrared spectra (FTIR) for all systems under study, where the spectra corresponding to the layers that have been attacked by the NH_4NO_3 solution are represented.

In general, for CEM IV system (Fig. 13a), the presence of characteristic vibration bands of the cementitious systems are identified, such as: carbonates (1470 cm^{-1}, 1420 cm^{-1}, and 714 cm^{-1}) and ettringite (main band around 1114 cm^{-1}) [65]. The formation of the main hydration product (C–S–H/C-A-S-H gel) can also be identified in FTIR spectra by the formation of an asymmetric stretching vibration band of Si–O bonds around 970 cm^{-1} [65].

As the outer layers are more exposed to reaction with NH_4NO_3, further decalcification occurs. This can be confirmed by the position of the band centred around 970 cm^{-1} (NAL6 layer), which changes to higher wavenumber values up to about 1007 cm^{-1} (AL1 layer). This band change is indicative that C–S–H gel is richer in silicon, as a consequence of the loss of calcium from the gel itself [66]. As previously mentioned, a reaction occurs between NH_4NO_3 and the C–S–H gel, thus modifying its structure during the process. Thus, by using FTIR, it can be observed how the outer layers are the ones that have undergone the most decalcification of the C–S–H gel (see Fig. 13a).

Regarding the carbonate bands, around 1470 cm^{-1}, a slight decrease in the intensity of this band is also observed as the leaching process takes place (see Fig. 13b). If this band is compared for the NAL6 layer (non-attacked zone) with the AL1 (outermost and at-

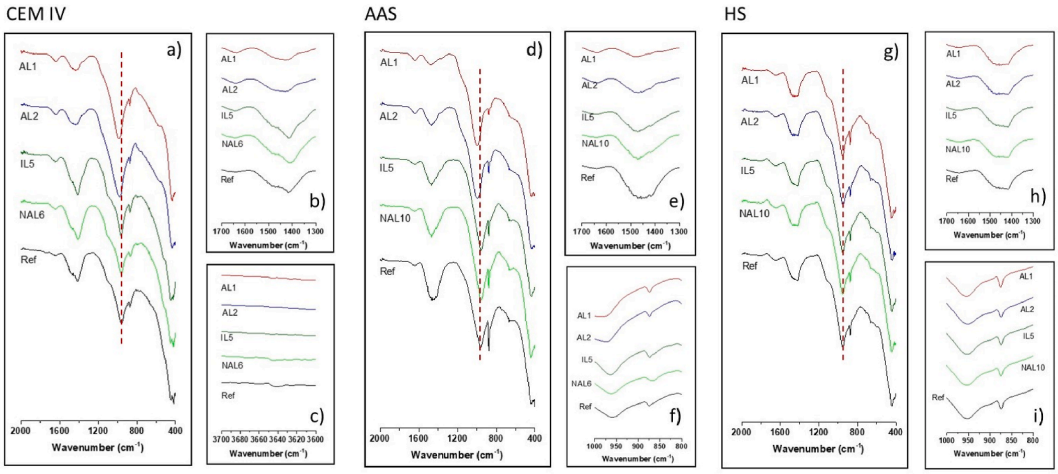

Fig. 13. FTIR spectra for: **a)** CEM IV between 2000 and 400 cm^{-1}, **b)** FTIR region between 1700 and 1300 cm^{-1} corresponding to the presence of carbonates; **c)** FTIR region between 3700 and 3600 cm^{-1} corresponding to the presence of portlandite; **d)** AAS between 2000 and 400 cm^{-1}; **e)** FTIR region between 1700 and 1300 cm^{-1} corresponding to the presence of carbonates; **f)** FTIR region between 1000 and 800 cm^{-1} corresponding to the presence of C-A-S-H gel; **g)** HS between 2000 and 400 cm^{-1}; **h)** FTIR region between 1700 and 1300 cm^{-1} corresponding to the presence of carbonates; **i)** FTIR region between 1000 and 800 cm^{-1} corresponding to the presence of C–S–H/C-A-S-H gel.

tacked zone), it can be seen how the calcium present in the $CaCO_3$ (calcite type) has reacted with the NH_4NO_3 solution, thus causing the decalcification of the sample.

In addition, in the FTIR spectra of CEM IV (reference sample), a slight band is observed around 3640 cm^{-1}, characteristic of the presence of portlandite (see Fig. 13c). It can be seen how this band disappears completely as the attack front advances, being somewhat more present in the NAL6 sample (interphase zone). However, in layers AL1 and AL2, there is no evidence of this band.

A slight change can also be observed in the band around 1110 cm^{-1}, mainly attributed to the presence of ettringite (asymmetric vibrations of the S - O bonds). Its low intensity is more noticeable in the internal layers of the sample (NAL6 and IL5), where a slight shoulder is visible. When the sample reacts with the decalcifying solution, a considerable destabilization of the ettringite is confirmed. This band is therefore completely absent in layers AL1.

FTIR spectra of the AAS pastes at different zones are shown in Fig. 13d. The absorption bands observed at 960–1020 cm^{-1} were associated to asymmetrical stretching vibrations of Si–O bonds in C–A–S–H gel [67]. It is evident that this band increases the wavenumber for the attacked layers (AL1, AL2) due to the decalcification that these layers undergo [68]. The bands at 1630 cm^{-1} were associated with the H–O–H bending vibration in water [69]. The band at around 450 cm^{-1} was attributed to Si–O–Si bond vibration while the bands at 670 cm^{-1} were due to the stretching vibrations generated by the Al–O bonds in the AlO_4 groups [54]. As in the CEM IV system, a displacement of the band towards higher wavenumber values is observed in zones that are attacked with the NH_4NO_3 solution, indicative of the decalcification of the C-A-S-H gel and therefore, the formation of a gel richer in silicon. Something similar occurs with the band corresponding to the presence of carbonates, located around 1470 cm^{-1}. As the attack front evolves, it is observed how the intensity of said band decreases, indicating that the Ca-rich species (calcite type) are also being leached. This fact could be verified by XRD (see Fig. 11b).

For HS systems, FTIR spectra are shown in Fig. 13h. Bands belonging to carbonates (1420 cm^{-1}) and ettringite (main band around 1120 cm^{-1}) [65] are present due to the amount of CEM I that this system contains (see Table 2). As mentioned above for CEM IV, the ettringite band disappears for the attacked layers (AL1 and AL2) due to leaching and this was confirmed by XRD (Fig. 11c). The formation of the main hydration product (C–S–H or C-A-S–H gel) can also be identified in FTIR spectra (see Fig. 13g) by the formation of an asymmetric vibration band of Si–O bonds around 960 cm^{-1} [65]. Finally, the band at around 450 cm^{-1} was attributed to Si–O–Si bond vibration while the bands at 670 cm^{-1} was due to the stretching vibrations generated by the Al–O bonds in the AlO_4 groups [54].

4. Conclusions

The conclusions to be drawn from the findings reported and analyzed above are as follows.

- The decalcification rate (regardless of the system evaluated) is higher during the first days of exposure, due to the high reactivity of portlandite with ammonium nitrate. Decalcification of portlandite in the first layers occurs long before the decalcification of C–S–H or C–A–S–H gels in deeper layers. Regarding the mineralogical and microstructural characterization, the layers most exposed to the solution showed decalcification of the main reaction products formed after the hydration of the cements and by-products, such as: C–S–H or C-(A)-S-H gels, portlandite and ettringite. In addition, it was also found that the anhydrous phases present in all systems reacted with the ammonium nitrate leaching solution.
- CEM IV pastes undergo the highest decalcification of the studied materials as of the first day immersed in the leaching solution, due to their higher content of C–S–H and C-A-S-H gels, portlandite and ettringite.

- AAS showed significantly higher resistance to decalcification in relation to the Portland cement CEM IV, mainly due to the absence of portlandite and the high level of polymerization of silicate chains. In addition, this AAS system is more resistant because of the microstructure of the sample, since it is much less porous and there is also a refinement of the structure as the attack with ammonium nitrate occurs.
- The HS system presents a behaviour similar to that of the CEM IV in terms of the microstructure formed after the leaching process. The incorporation of Na_2SO_4 as an activator plays an important role in the leaching mechanism, since the sulfur present is leached in large quantities and, in addition, new hydration phases affecting the microstructure are formed, such as gypsum.

Author statement

S. Shagñay: Conceptualization, Methodology, Formal analysis, Software, Writing – original draft, Writing – review & editing. **I. Garcia-Lodeiro:** Conceptualization, Investigation, Resources, Formal analysis, Data curation, Writing – original draft, Supervision. **F. Velasco:** Conceptualization, Writing – review & editing, Validation, Supervision, Funding acquisition. **A. Bautista:** Conceptualization, Resources, Writing – original draft, Validation, Supervision, Funding acquisition, Writing – review & editin. **M. Torres-Carrasco:** Conceptualization, Resources, Writing – original draft, Validation, Supervision, Funding acquisition, Writing – review & editin.

Declaration of competing interest

The authors declare the following financial interests/personal relationships which may be considered as potential competing interests: Asuncion Bautista reports financial support was provided by University Carlos III of Madrid. Asuncion Baustista reports a relationship with University Carlos III of Madrid that includes: board membership and employment.

Data availability

Data will be made available on request.

Acknowledgements

The authors have been able to carry out the present research thanks to financial support from the Ministerio de Ciencia, Innovación y Universidades of Spain (RTI2018-096428-B-I00 and PID2020-116738RJ-I00 projects) and Madrid Government (Comunidad de Madrid) under the Multiannual Agreement UC3M in the line of “Fostering Young Doctors Research” (HORATSO–CS–UC3M) in the context of the V PRICIT (Regional Programme of Research and Technological Innovation).

References

[1] C. Bataille, Low and zero emissions in the steel and cement industries, in: Green Growth Sustain. Dev. Forum, Paris, 2007, pp. 1–41. http://oe.cd/ggsd2019.
[2] G.U. Fayomi, S.E. Mini, O.S.I. Fayomi, A.A. Ayoola, Perspectives on environmental CO_2 emission and energy factor in cement industry, IOP Conf. Ser. Earth Environ. Sci. 331 (2019), https://doi.org/10.1088/1755-1315/331/1/012035.
[3] N.A. Madlool, R. Saidur, M.S. Hossain, N.A. Rahim, A critical review on energy use and savings in the cement industries, Renew. Sustain. Energy Rev. 15 (2011) 2042–2060, https://doi.org/10.1016/j.rser.2011.01.005.
[4] A. Mian, M. Bendig, G. Piazzesi, G. Manente, A. Lazzaretto, F. Maréchal, Energy Integration in the cement industry, in: Comput. Aided Chem. Eng., Elsevier, 2013, pp. 349–354, https://doi.org/10.1016/B978-0-444-63234-0.50059-2.
[5] P.A. Claisse, Cements and cement replacement materials, in: Civ. Eng. Mater., Butterworth-Heinemann, 2016, pp. 163–176, https://doi.org/10.1016/b978-0-08-100275-9.00018-8.
[6] M. Glavind, Sustainability of cement, concrete and cement replacement materials in construction, in: Sustain. Constr. Mater., Woodhead Publishing, 2009, pp. 120–147, https://doi.org/10.1533/9781845695842.120.
[7] J.L. Provis, Alkali-activated materials, Cement Concr. Res. 114 (2018) 40–48, https://doi.org/10.1016/j.cemconres.2017.02.009.
[8] J. Zhang, C. Shi, Z. Zhang, Z. Ou, Durability of alkali-activated materials in aggressive environments: a review on recent studies, Construct. Build. Mater. 152 (2017) 598–613, https://doi.org/10.1016/j.conbuildmat.2017.07.027.
[9] M. Alhawat, A. Ashour, G. Yildirim, A. Aldemir, M. Sahmaran, Properties of geopolymers sourced from construction and demolition waste: a review, J. Build. Eng. 50 (2022) 104104, https://doi.org/10.1016/j.jobe.2022.104104.
[10] M. Torres-Carrasco, J.G. Palomo, F. Puertas, Sodium silicate solutions from dissolution of glasswastes. Statistical analysis, Mater. Construcción 64 (2014), https://doi.org/10.3989/mc.2014.05213.
[11] F. Puertas, M. Torres-Carrasco, Use of glass waste as an activator in the preparation of alkali-activated slag. Mechanical strength and paste characterisation, Cement Concr. Res. 57 (2014) 95–104, https://doi.org/10.1016/j.cemconres.2013.12.005.
[12] Z. Tang, W. Li, Y. Hu, J.L. Zhou, V.W.Y. Tam, Review on designs and properties of multifunctional alkali-activated materials (AAMs), Construct. Build. Mater. 200 (2019) 474–489, https://doi.org/10.1016/j.conbuildmat.2018.12.157.
[13] S. Çelikten, M. Sarıdemir, İ. Özgür Deneme, Mechanical and microstructural properties of alkali-activated slag and slag + fly ash mortars exposed to high temperature, Construct. Build. Mater. 217 (2019) 50–61, https://doi.org/10.1016/j.conbuildmat.2019.05.055.
[14] S. Shagñay, F. Velasco, A. del Campo, M. Torres-Carrasco, Wear behavior in pastes of alkali-activated materials: influence of precursor and alkali solution, Tribol. Int. 147 (2020), https://doi.org/10.1016/j.triboint.2020.106293.
[15] M. Shariati, A. Shariati, N.T. Trung, P. Shoaei, F. Ameri, N. Bahrami, S.N. Zamanabadi, Alkali-activated slag (AAS) paste: correlation between durability and microstructural characteristics, Construct. Build. Mater. 267 (2021) 120–886, https://doi.org/10.1016/j.conbuildmat.2020.120886.
[16] D. Shi, J. Ye, W. Zhang, Effects of activator content on properties, mineralogy, hydration and microstructure of alkali-activated materials synthesized from calcium silicate slag and ground granulated blast furnace slag, J. Build. Eng. 32 (2020) 101791, https://doi.org/10.1016/j.jobe.2020.101791.
[17] A. Aboulayt, F. Souayfan, E. Roziere, R. Jaafri, A. Cherki El Idrissi, R. Moussa, C. Justino, A. Loukili, Alkali-activated grouts based on slag-fly ash mixtures: from early-age characterization to long-term phase composition, Construct. Build. Mater. 260 (2020) 120510, https://doi.org/10.1016/j.conbuildmat.2020.120510.
[18] S. Fernando, C. Gunasekara, D.W. Law, M.C.M. Nasvi, S. Setunge, R. Dissanayake, Engineering properties of waste-based alkali activated concrete brick containing low calcium fly ash and rice husk ash: a comparison with traditional Portland cement concrete brick, J. Build. Eng. 46 (2022) 103810, https://doi.org/10.1016/j.jobe.2021.103810.

[19] E. Batuecas, I. Ramón-Álvarez, S. Sánchez-Delgado, M. Torres-Carrasco, Carbon footprint and water use of alkali-activated and hybrid cement mortars, J. Clean. Prod. 319 (2021) 128–653, https://doi.org/10.1016/j.jclepro.2021.128653.
[20] C.K. Yip, G.C. Lukey, J.S.J. Van Deventer, The coexistence of geopolymeric gel and calcium silicate hydrate at the early stage of alkaline activation, Cement Concr. Res. 35 (2005) 1688–1697, https://doi.org/10.1016/j.cemconres.2004.10.042.
[21] C. Shi, A. Fernández-Jiménez, A. Palomo, New cements for the 21st century: the pursuit of an alternative to Portland cement, Cement Concr. Res. 41 (2011) 750–763, https://doi.org/10.1016/j.cemconres.2011.03.016.
[22] Á. Palomo, O. Maltseva, I. García-Lodeiro, A. Fernández-Jiménez, Hybrid alkaline cements. Part II: the clinker factor, Rev. Rom. Mater. Rom. J. Mater. 43 (2013) 74–80.
[23] I. Garcia-Lodeiro, O. Maltseva, A. Palomo, A. Fernández-Jiménez, Hybrid alkaline cements. Part I: fundamentals, in: rom, J. Mater. (2012) 330–335.
[24] S. Shagñay, A. Butista, F. Velasco, M. Torres-Carrasco, Hybrid cements: towards their use as alternative and durable materials against wear, Construct. Build. Mater. 312 (2021) 125397, https://doi.org/10.1016/J.CONBUILDMAT.2021.125397.
[25] I. Ramón-Álvarez, C. Marugán-Cruz, E. Enríquez, S. Sánchez-Delgado, M. Torres-Carrasco, Alkali-activated and hybrid materials: alternative to Portland cement as a storage media for solar thermal energy, Bol. La Soc. Esp. Ceram. y Vidr. (2021), https://doi.org/10.1016/j.bsecv.2021.11.006.
[26] S. Shagñay, L. Ramón, M. Fernández-Álvarez, A. Bautista, F. Velasco, M. Torres-Carrasco, Eco-efficient hybrid cements: pozzolanic, mechanical and abrasion properties, Appl. Sci. 10 (2020) 1–15, https://doi.org/10.3390/app10248986.
[27] C. Le Bellego, B. Gerard, G. Pijaudier-Cabot, Chemo-mechanical effects in mortars beams subjected to water hydrolysis, J. Eng. Mech. 126 (2000) 266–272, https://doi.org/10.1061/(ASCE)0733-9399(2000)126:3(266).
[28] R.E. Beddoe, W. Müllauer, D. Heinz, On leaching mechanisms of major and trace elements from concrete - carbonation, exposure to deicing salt and external sulphates, J. Build. Eng. 45 (2022) 103435, https://doi.org/10.1016/j.jobe.2021.103435.
[29] C. Perlot, M. Carcassès, J. Verdier, Diffusivity evolution under decalcification: influence of aggregate natures and cement type, Mater. Struct. Constr. 46 (2013) 787–801, https://doi.org/10.1617/s11527-012-9934-y.
[30] F.P. Glasser, J. Marchand, E. Samson, Durability of concrete - degradation phenomena involving detrimental chemical reactions, Cement Concr. Res. 38 (2008) 226–246, https://doi.org/10.1016/j.cemconres.2007.09.015.
[31] I. Garcia-Lodeiro, G. Goracci, J. Dolado, M. Blanco-Varela, Mineralogical and microstructural alterations in a portland cement paste after an accelerated decalcification process, Cement Concr. Res. 140 (2021) 106312, https://doi.org/10.1016/j.cemconres.2020.106312.
[32] F. Puertas, S. Goñi, M.S. Hernández, C. Varga, A. Guerrero, Comparative study of accelerated decalcification process among C3S, grey and white cement pastes, Cem. Concr. Compos. 34 (2012) 384–391, https://doi.org/10.1016/J.CEMCONCOMP.2011.11.002.
[33] Q.T. Phung, N. Maes, D. Jacques, G. De Schutter, G. Ye, Investigation of the changes in microstructure and transport properties of leached cement pastes accounting for mix composition, Cement Concr. Res. 79 (2016) 217–234, https://doi.org/10.1016/j.cemconres.2015.09.017.
[34] C. Carde, R. François, J.M. Torrenti, Leaching of both calcium hydroxide and C-S-H from cement paste: modeling the mechanical behavior, Cement Concr. Res. 26 (1996) 1257–1268, https://doi.org/10.1016/0008-8846(96)00095-6.
[35] H. Bilal, T. Chen, M. Ren, X. Gao, A. Su, Influence of silica fume, metakaolin & SBR latex on strength and durability performance of pervious concrete, Construct. Build. Mater. 275 (2021) 122124, https://doi.org/10.1016/j.conbuildmat.2020.122124.
[36] F. Yang, F. Pang, J. Xie, W. Wang, W. Wang, Z. Wang, Leaching and solidification behavior of Cu2+, Cr3+ and Cd2+ in the hydration products of calcium sulfoaluminate cement, J. Build. Eng. 46 (2022) 103696, https://doi.org/10.1016/j.jobe.2021.103696.
[37] F. Adenot, M. Buil, Modelling of the corrosion of the cement paste by deionized water, Cement Concr. Res. 22 (1992) 489–496, https://doi.org/10.1016/0008-8846(92)90092-A.
[38] M. Jebli, F. Jamin, E. Garcia-Diaz, M. El Omari, M.S. El Youssoufi, Influence of leaching on the local mechanical properties of an aggregate-cement paste composite, Cem. Concr. Compos. 73 (2016) 241–250, https://doi.org/10.1016/j.cemconcomp.2016.05.001.
[39] C. Carde, G. Escadeillas, R. François, Use of ammonium nitrate solution to simulate and accelerate the leaching of cement pastes due to deionized water, Mag. Concr. Res. 49 (1997) 295–301, https://doi.org/10.1680/macr.1997.49.181.295.
[40] I. Arribas, I. Vegas, V. García, R. Vigil de la Villa, S. Martínez-Ramírez, M. Frías, The deterioration and environmental impact of binary cements containing thermally activated coal mining waste due to calcium leaching, J. Clean. Prod. 183 (2018) 887–897, https://doi.org/10.1016/j.jclepro.2018.02.127.
[41] F.M. Lea, The action of ammonium salts on concrete, Mag. Concr. Res. 17 (1965) 115–116, https://doi.org/10.1680/macr.1965.17.52.115.
[42] K. Wan, L. Li, W. Sun, Solid-liquid equilibrium curve of calcium in 6 mol/L ammonium nitrate solution, Cement Concr. Res. 53 (2013) 44–50, https://doi.org/10.1016/j.cemconres.2013.06.003.
[43] A. Bouchikhi, Y. Mamindy-Pajany, W. Maherzi, C. Albert-Mercier, H. El-Moueden, M. Benzerzour, A. Peys, N.E. Abriak, Use of residual waste glass in an alkali-activated binder – structural characterization, environmental leaching behavior and comparison of reactivity, J. Build. Eng. 34 (2021) 101903, https://doi.org/10.1016/j.jobe.2020.101903.
[44] S. Goñi, M. Frías, R.V. De La Villa, I. Vegas, Decalcification of activated paper sludge - fly ash-Portland cement blended pastes in pure water, Cem. Concr. Compos. 40 (2013) 1–6, https://doi.org/10.1016/j.cemconcomp.2013.04.002.
[45] L. Zampori, P.G. Stampino, G. Dotelli, Long-term leaching test of organo-contaminated cement-clay pastes, J. Hazard Mater. 170 (2009) 1041–1049, https://doi.org/10.1016/j.jhazmat.2009.05.076.
[46] S. Park, H.N. Yoon, J. Seo, H.K. Lee, J.G. Jang, Structural evolution of binder gel in alkali-activated cements exposed to electrically accelerated leaching conditions, J. Hazard Mater. 387 (2020) 121825, https://doi.org/10.1016/j.jhazmat.2019.121825.
[47] F.H. Heukamp, F.J. Ulm, J.T. Germaine, Mechanical properties of calcium-leached cement pastes: triaxial stress states and the influence of the pore pressures, Cement Concr. Res. 31 (2001) 767–774, https://doi.org/10.1016/S0008-8846(01)00472-0.
[48] T.C.56-M.H.M. Rilem, CPC-18 measurement of hardened concrete carbonation depth, Mater. Struct. 21 (1988) 453–455, https://doi.org/10.1617/2351580117.026.
[49] S. Shagñay, A. Bautista, F. Velasco, M. Torres-Carrasco, Carbonation of alkali-activated and hybrid mortars manufactured from slag: confocal Raman microscopy study and impact on wear performance, Boletín La Soc. Española Cerámica y Vidr. (2022), https://doi.org/10.1016/J.BSECV.2022.07.003.
[50] H. Justnes, T.A. Østnor, Designing alternative binders utilizing synergic reactions, in: Roceedings NTCC 2014, 5th Int. Conf. Non-traditional Cem. Concr., Vysoké učení technické, Brno, Czech Republic, 2014, pp. 101–104 978-80-214-4867-4.
[51] V. Bílek, L. Kalina, R. Novotnỳ, J. Tkacz, L. Pařízek, Some issues of shrinkage-reducing admixtures application in alkali-activated slag systems, Materials 9 (2016), https://doi.org/10.3390/ma9060462.
[52] H. Ye, A. Radlińska, Shrinkage mechanisms of alkali-activated slag, Cement Concr. Res. 88 (2016) 126–135, https://doi.org/10.1016/j.cemconres.2016.07.001.
[53] B. Zhang, H. Zhu, P. Feng, P. Zhang, A review on shrinkage-reducing methods and mechanisms of alkali-activated/geopolymer systems: effects of chemical additives, J. Build. Eng. 49 (2022) 104056, https://doi.org/10.1016/j.jobe.2022.104056.
[54] F. Puertas, M. Torres-Carrasco, Use of glass waste as an activator in the preparation of alkali-activated slag. Mechanical strength and paste characterisation, Cement Concr. Res. 57 (2014) 95–104, https://doi.org/10.1016/j.cemconres.2013.12.005.
[55] N. Alharbi, B. Varela, R. Hailstone, Alkali-activated slag characterization by scanning electron microscopy, X-ray microanalysis and nuclear magnetic resonance spectroscopy, Mater. Char. 168 (2020) 110504, https://doi.org/10.1016/j.matchar.2020.110504.
[56] M.M. Komljenović, Z. Baščarević, N. Marjanović, V. Nikolić, Decalcification resistance of alkali-activated slag, J. Hazard Mater. 233–234 (2012) 112–121, https://doi.org/10.1016/j.jhazmat.2012.06.063.
[57] M. Alexander, A. Bertron, N. De Belie, Performance of cement-based materials in aggressive aqueous environments, RILEM State-of-the-Art Reports 10 (2013) 3–443, https://doi.org/10.1007/978-94-007-5413-3_13.
[58] H.T. Türker, M. Balçikanli, I.H. Durmuş, E. Özbay, M. Erdemir, Microstructural alteration of alkali activated slag mortars depend on exposed high temperature level, Construct. Build. Mater. 104 (2016) 169–180, https://doi.org/10.1016/j.conbuildmat.2015.12.070.
[59] H.Y. Zhang, V. Kodur, B. Wu, L. Cao, F. Wang, Thermal behavior and mechanical properties of geopolymer mortar after exposure to elevated temperatures,

Construct. Build. Mater. 109 (2016) 17–24, https://doi.org/10.1016/j.conbuildmat.2016.01.043.
[60] Y. Cai, L. Yu, Y. Yang, Y. Gao, C. Yang, Effect of early age-curing methods on drying shrinkage of alkali-activated slag concrete, Materials 12 (2019), https://doi.org/10.3390/ma12101633.
[61] M. Thiery, G. Villain, P. Dangla, G. Platret, Investigation of the carbonation front shape on cementitious materials: effects of the chemical kinetics, Cement Concr. Res. 37 (2007) 1047–1058, https://doi.org/10.1016/j.cemconres.2007.04.002.
[62] K. Scrivener, R. Snellings, B. Lothenbach, F. Group, A Practical Guide to Microstructural Analysis of Cementitious Materials, CRC Press, Boca Raton, FL, USA, 2016, https://doi.org/10.1201/b19074.
[63] Y. Wang, Q. Yuan, D. Deng, Degradation of mechanical properties of CA mortar caused by calcium leaching, Construct. Build. Mater. 208 (2019) 613–621, https://doi.org/10.1016/j.conbuildmat.2019.02.164.
[64] K. Scrivener, R. Snellings, B. Lothenbach, F. Group, A Practical Guide to Microstructural Analysis of Cementitious Materials, 2018, https://doi.org/10.1201/b19074.
[65] M. Torres-Carrasco, A. Campo, M.A. De Rubia, E. Reyes, A. Moragues, J.F. Fernández, New insights in weathering analysis of anhydrous cements by using high spectral and spatial resolution Confocal Raman Microscopy, Cement Concr. Res. 100 (2017) 119–128, https://doi.org/10.1016/j.cemconres.2017.06.003.
[66] V. Colin-Farmer, in: V.C. farmer (Ed.), The Infrared Spectra of Minerals, mineralogical society, 1975, https://doi.org/10.1016/S0003-2670(00)00181-1.
[67] F. Puertas, M. Palacios, H. Manzano, J.S. Dolado, A. Rico, J. Rodríguez, A model for the C-A-S-H gel formed in alkali-activated slag cements, J. Eur. Ceram. Soc. 31 (2011) 2043–2056, https://doi.org/10.1016/j.jeurceramsoc.2011.04.036.
[68] H. Peng, C. Cui, Z. Liu, C.S. Cai, Y. Liu, Synthesis and reaction mechanism of an alkali-activated metakaolin-slag composite system at room temperature, J. Mater. Civ. Eng. 31 (2019) https://doi.org/10.1061/(asce)mt.1943-5533.0002558, 04018345.
[69] I. Lecomte, C. Henrist, M. Liégeois, F. Maseri, A. Rulmont, R. Cloots (Micro)-structural comparison between geopolymers, alkali-activated slag cement and Portland cement, J. Eur. Ceram. Soc. 26 (2006) 3789–3797, https://doi.org/10.1016/j.jeurceramsoc.2005.12.021.